Electron spin resonance parameters of bulk oxygen vacancy in semiconducting tin dioxide

Nergiz Özcan,[1] Tommi Kortelainen,[2] Vyacheslav Golovanov,[3] Tapio T. Rantala,[2] and Juha Vaara[4,1,*]

[1]*Laboratory of Physical Chemistry, Department of Chemistry, University of Helsinki, P.O. Box 55 (A.I. Virtasen aukio 1), FIN-00014 Helsinki, Finland*

[2]*Department of Physics, Tampere University of Technology, P.O. Box 692, FIN-33101 Tampere, Finland*

[3]*South-Ukrainian University, Staroportofrankovskaya Str. 26, 65008 Odessa, Ukraine*

[4]*NMR Research Group, Department of Physics, University of Oulu, P.O. Box 3000, FIN-90014 Oulu, Finland*

(Received 25 August 2009; revised manuscript received 3 May 2010; published 3 June 2010)

We present density-functional theory calculations of the electron spin resonance g and hyperfine coupling $\boldsymbol{A}$ tensors in cluster models of a positively charged oxygen vacancy V_O^+ in semiconducting tin dioxide, SnO_2. Convergence of the results with the cluster size, basis set, choice of exchange-correlation functional, and choice of the method of the cluster termination by either pseudohydrogen atoms or electrostatic embedding, are investigated. The results agree with two of the earlier experimental assignments of the g value around 2.00, whereas in the case of other experiments ($g=1.89$), a reassignment is suggested. We also investigate the energy levels of the impurity states via the Kohn-Sham orbital energies of the defect-free bulk, positively charged vacancy (V_O^+), and neutral vacancy (V_O^0) structures.

DOI: 10.1103/PhysRevB.81.235202 PACS number(s): 76.30.Mi, 71.20.Nr, 72.20.Jv

I. INTRODUCTION

The electric conductivity of SnO_2 is sensitive to the composition of the surrounding atmosphere, facilitating the use of this material in solid-state gas sensors.[1] Conventionally, this is related to the oxygen surface chemistry at the grain boundaries and the charge carrier density of this wide band-gap semiconductor and, in particular, the interplay of these two. Traditionally, the semiconducting behavior is thought to arise from the high density of intrinsic defects and donors, such as bulk oxygen vacancies and Sn interstitials,[2,3] although this view has recently been challenged.[4] Not only the charge density but also spin-density redistribution may take place at the defect sites. Thus, electron spin resonance (ESR) is an efficient experimental method to investigate properties of such defects, as modeling and calculation of the electronic structure allows detailed interpretation.[5] The ESR parameters (g and hyperfine tensors, $\boldsymbol{A}$) can be directly calculated for cluster models using quantum-chemical tools. Calculation of properties depending on the external magnetic field $\boldsymbol{B}_0$, such as the g tensor, face formal and practical complications when calculated using periodic methods, although such approaches are emerging.[6,7] The corresponding magnetic vector potential $\boldsymbol{\mathcal{A}}_0$ is a nonperiodic function of spatial coordinates. Furthermore, the conventional plane-wave basis sets of periodic calculations are not equally well suited for hyperfine properties as localized, e.g., Gaussian basis sets. Embedded cluster models facilitate using the well-established quantum-chemical tools, high-level calculations of the often rather localized magnetic properties of defects in fairly large clusters. Finite models also eliminate the interaction of defects with their periodic images, for charged defects there is no need to apply a constant background charge, and one benefits from having a well-defined spin multiplicity.

The paramagnetic centers in metal and metal oxide nanoparticles can be used for immobilization of bioactive probes with interesting applications in nanomedicine.[8,9] In addition, recent studies show that tin oxide is a promising material for spintronics applications.[10] Therefore, the investigation of spin-polarized states in tin oxide nanoparticles has become a priority. However, at present there are some discrepancies concerning the structure of such paramagnetic centers. Ivanovskaya *et al.*[11] and Popescu *et al.*[12] attributed the weak ESR signal with the g factor around 2.00 to a singly ionized oxygen vacancy (V_O^+) in the crystal lattice. By contrast, Canevali *et al.*[13,14] associate V_O^+ with a symmetrical resonance line observed at $g=1.89$. On the other hand, according to calculations of Ágoston *et al.*[3] and Singh *et al.*,[4] the V_O^+ defect is unstable and the oxygen vacancies should typically exist in the ESR-silent neutral V_O^0 or doubly ionized V_O^{2+} charge states only. There is obvious lack of theoretical information on the microscopic structure and properties of the relevant paramagnetic defects. It is evident that consistent first-principles models are necessary for further systematic study of such centers in SnO_2. In these density-functional theory (DFT) calculations, the electronic levels and ESR spectroscopic parameters can be calculated independently of the experiments. This facilitates a direct and unbiased comparison of experiment and theory, and hopefully identification of the ESR defects.

In the present paper we construct cluster models for the paramagnetic oxygen vacancy, V_O^+ in SnO_2, compute the electronic structure, g tensor and isotropic hyperfine couplings A, and relate the findings to the experimental data. Besides resolving the issue of the g value being either 2.002–2.005 (Refs. 11 and 12) or 1.89 (Refs. 13 and 14), we investigate the structure of the Kohn-Sham energy levels in the cluster models of the oxygen vacancy.

II. METHODS

A. Periodic calculations

We start with a bulk SnO_2 calculation with periodic boundary conditions (PBC). A unit cell Sn_4O_8 is chosen for convenience of future modeling of the surface of the crystal,

instead of the conventional primitive cell Sn_2O_4 with different orientation. This choice will in the future allow us modeling of the most abundant (110) surface using the same orientation in the slab model. These issues are discussed in Ref. 15 in more detail. The computational supercell of $(Sn_4O_8)_4$ is a $1\times4\times1$ multiple of the chosen unit cell, thus containing 48 atoms.

The first-principles DFT approach used here is based on the plane-wave basis set and the pseudopotential concept to describe the electron-ion interaction (CASTEP code[16,17]). The ultrasoft pseudopotentials[18] used for atomic cores leave six and four active electrons for the oxygen and tin atoms, respectively. Thus, we have 256 electrons to deal with in the calculation. The plane-wave basis convergence was found below 380 eV, which is used as the cutoff. The Brillouin zone is sampled with $2\times2\times4$ Monkhorst-Pack k points.[19] Electronic exchange and correlation are included by the Perdew-Burke-Ernzerhof generalized-gradient approximation (GGA) (PBE).[20] The spin-polarized version[21] is used here.

The purpose of these PBC calculations is to obtain good geometries for the oxygen defects. Therefore, a careful structural relaxation to the minimum energy was carried out, first for the bulk to obtain a basic reference. As we model isolated defects, the found supercell lattice constants $6.64\times12.57\times6.70$ Å^3 were used for both the neutral and ionized vacancy model, which were internally fully relaxed.

B. Cluster model construction

The optimized unit cells from periodic calculations of the bulk SnO_2 structure were first replicated to make a very large cluster in order to setup the lattice sites for both the quantum mechanically treated cluster and embedding charges. We selected three different sizes for the quantum cluster. The defined, nonstoichiometric quantum clusters contain 3 tin and 15 oxygen atoms, 7 tin and 29 oxygen atoms, and 12 tin and 48 oxygen atoms, denoted Sn3, Sn7, and Sn12, respectively. These clusters correspond to imposing for the first, second, and third layer of tin atoms around the vacancy site, the correct coordination with six oxygen atoms. In the case of the vacancy there is one missing oxygen at the center of the quantum cluster (Fig. 1). Relaxed atom positions from the periodic calculations of the V_O^0 and V_O^+ models were chosen for the atoms that are within the distance of 5 Å from the vacancy. The atomic positions from the periodic optimization of the defect-free lattice were adopted for the atoms further away from the vacancy. By this procedure we cannot capture any long-range structural relaxation effects around the defect, which would require either a very large supercell to be used in periodic calculations or a polarizable shell model in cluster calculations.[22] According to the CASTEP optimization of the defect models, the atoms at the distance of 5 Å from the vacancy typically relax by about 0.01 Å as compared to the bulk structure.

Different embedding methods were used. As a first model, we used hydrogen termination of the dangling bonds from the O atoms at the perimeter of the cluster. Pseudohydrogen ($H^\star$) nuclei with $+2e/3$ charge were used to provide the

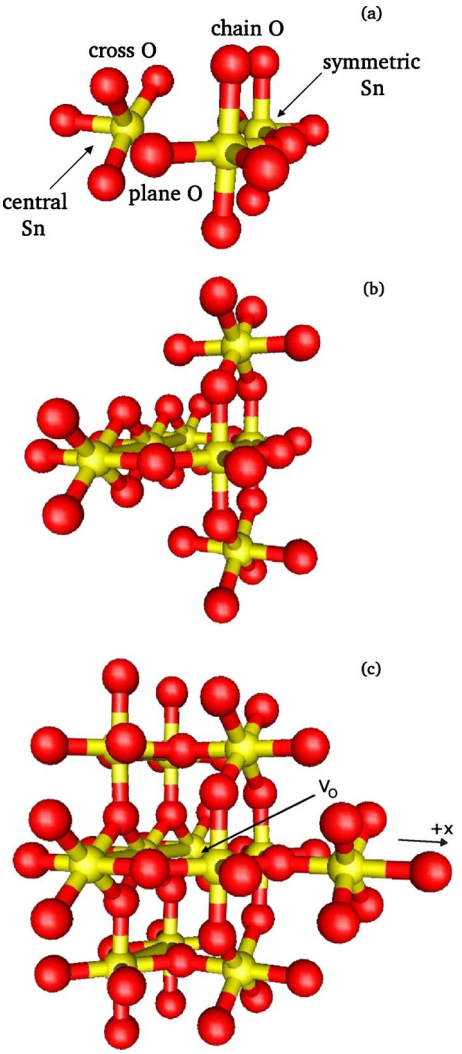

FIG. 1. (Color online) Cluster models of tin dioxide (a) Sn3, (b) Sn7, and (c) Sn12, respectively. Different types of oxygen and tin atoms in the neighborhood of the vacancy are named in (a). In (c), the arrow indicates the position of the vacancy. Also the direction $(+x)$ of the applied depolarization electric field is indicated.

correct oxidation state for the perimeter oxygen atoms around the quantum cluster.[23] These pseudohydrogen atoms were placed in the original direction of the bond at the distance of 1 Å.

In another method, embedding by point charges was used to reproduce the periodic Madelung potential of the defect-free, optimized SnO_2 structure within the volume of the quantum cluster (Fig. 2). We used the method and program EWALD of Refs. 24 and 25, where two shells of point charges are placed around the quantum cluster. The first layer, the so-called fixed zone, contains the formal charges $q_O=-2e$, $q_{Sn}=+4e$ at the lattice points of the defect-free structure. The second layer, the so-called parameter zone, contains point charges with least-squares fitted values. For example, about 3000 and 38 000 point charges were used in the fixed and parameter zones, respectively, to fit the Madelung potential of the Sn12 cluster to within 1 μV at the lattice points within the quantum cluster and the fixed zone, as well as at 1000 random points within the quantum cluster.

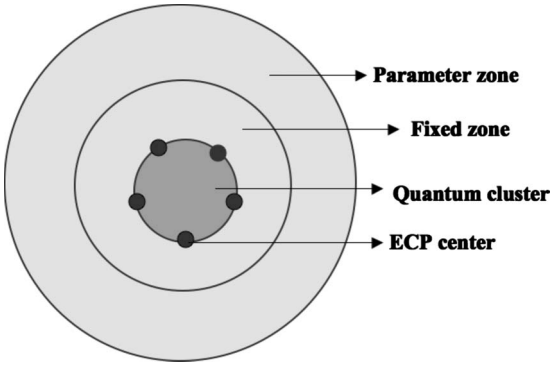

FIG. 2. Schematic image of the shells around the quantum cluster in the embedded cluster calculations. See text for details.

Point-charge embedding involves charge leakage from the quantum cluster to the neighboring cationic point charges.[26] In order to reduce this effect, effective core potential (ECP) centers, without electrons or basis functions were placed at the cationic Sn sites at the borderline between the quantum cluster and the fixed zone. We used the four valence-electron, energy-consistent Stuttgart ECPs for this purpose.[27]

Finite cluster models of ionic solids suffer from the generation of spurious electric dipole moment and an associated electric field due to uncompensated surface charges.[28] To approximately eliminate these effects, we apply a finite, homogeneous electric field [finite-field (ff)] in our final cluster models. The direction [Fig. 1(c)] and magnitude of the field was calibrated to result in vanishing force on the central oxygen atom in the differently sized embedded cluster models of bulk SnO_2. Essentially the same ff-EWALD-ECP embedding method was recently employed for the ^{17}O nuclear magnetic resonance shielding tensors in perovskite materials.[28]

C. ESR calculations

For a general reference to the theory of ESR parameters, see Ref. 29. We calculated the $\boldsymbol{A}$ and g tensors for the V_O^+ model ($S=\frac{1}{2}$) using DFT within the GGA with the PBE exchange-correlation functional and the related hybrid functional PBE0.[20] The unrestricted Kohn-Sham formalism was employed.

The g tensor calculations were performed using the method implemented in the GAUSSIAN03 code,[30] earlier employed in Refs. 5, 31, and 32. The g tensor is written as a sum of four contributions. The electronic spin-Zeeman interaction contains a dominating contribution from the isotropic, free-electron g_e factor equal to 2.002319. The next term is an isotropic term arising from the "kinetic-energy correction" of the spin-Zeeman interaction. The third term is the gauge correction with an effective nuclear charge and where explicit two-electron contributions are omitted in the Gaussian implementation. These two terms are calculated as expectation values in the doublet ground state.[33] The last and most significant contribution to the deviation of the g tensor from the free-electron value is a second-order term involving the orbital Zeeman and spin-orbit interactions. The first of these operators mediates the perturbing effect of the external magnetic field to the wave function of the cluster, to be detected in the energy levels of the electron spin via the spin-orbit interaction.[34]

Concerning technical details, we used the NoVarAcc flag in the GAUSSIAN code in order to improve convergence by using the full integral accuracy from the very beginning of the optimization of the reference state. The grid=ultrafine flag was used for defining an accurate numerical integration grid.

Basis sets are detailed in Table I. We used the SVP (Ref. 35) polarized split-valence basis set as well as TZVP and TZVPP, triple-zeta valence basis sets extended by polarization functions.[36] The TZVP basis sets improves the description of both the core and valence properties as compared to SVP. The valence region is further improved by the additional polarization functions at the TZVPP level. The oxygen basis set was placed also at the vacancy site in order to enhance the basis-set convergence of the ESR parameters, similarly as in Ref. 37.

III. RESULTS AND DISCUSSION

A. One-electron levels

1. *Bulk* SnO_2

Table II lists the bulk band gaps calculated for the cluster models of different size, with H^* termination, EWALD-ECP embedding, and the variant of the latter with finite depolarization field (ff-EWALD-ECP). Figure 3(a) illustrates the calculated density of states (DOS) of the Sn12 model. For the bulk system, the gap decreases with increasing cluster size. Calculations performed with the EWALD-ECP model result in larger energy gaps than the H^*-termination model. Application of the finite-field results in a small downward adjustment of the gap value. The data obtained with the PBE0 hybrid functional are even larger than the corresponding PBE data. The H^*-termination model calculations coincide better with the experimental bulk energy gap value of 3.6 eV (Ref. 2). This is due to error cancellation between the lack of inclusion of the periodic potential in the H^*-termination model, the finite size of the clusters, and the

TABLE I. Number of basis functions used in the calculations.

Basis	Sn functions	O functions	Sn3	Sn7	Sn12
SVP	17*s*13*p*9*d*/6*s*5*p*3*d*	7*s*4*p*1*d*/3*s*2*p*1*d*	318	658	1104
TZVP	19*s*15*p*10*d*/8*s*7*p*6*d*	11*s*6*p*1*d*/5*s*3*p*1*d*	462	964	1620
TZVPP	19*s*15*p*11*d*1*f*/8*s*7*p*7*d*1*f*	11*s*6*p*2*d*1*f*/5*s*3*p*2*d*1*f*	678	1396	2340

TABLE II. Semiconducting gap and gap state energies (electron volt) for the EWALD-ECP and H*-termination models as functions of the cluster size for the models of bulk, neutral oxygen vacancy (V_O^0), and positively charged oxygen vacancy (V_O^+) in SnO_2. Values based on the Kohn-Sham orbital energies obtained using the TZVPP basis.

Embedding	Functional	Cluster size	Bulk gap	V_O^0 gap state[a]	$V_O^+\alpha$-gap state(1)[b]	$V_O^+\alpha$-gap state(2)[c]	$V_O^+\beta$-gap state(1)[d]	$V_O^+\beta$-gap state(2)[e]
H* term.	PBE	3	4.29	1.48	0.06	1.94	0.09	2.81
		7	3.90	1.67	0.04	1.19	0.05	2.06
		12	3.68	1.32	1.07	1.14	1.07	1.97
EWALD-ECP	PBE	3	6.07	2.20	0.09	2.71	0.13	3.70
		7	5.36	2.01	0.09	2.14	0.10	3.07
		12	4.83	1.77	1.04	1.64	1.04	2.52
	PBE0	12	7.53	2.55	1.13	2.34	1.13	4.92
ff-EWALD-ECP[f]	PBE	3	5.31	1.68		2.29		3.28
		7	4.84	1.69		1.48		2.41
		12	4.64	1.62		1.40		2.28
ff-EWALD-ECP[f]	PBE0	12	7.44	2.48		2.09		4.67

[a]Energy difference between the highest occupied molecular orbital, HOMO, and HOMO-1. HOMO is a doubly occupied impurity state in the middle of the gap. HOMO-1 is the top of the valence band.
[b]Energy difference between HOMO(α)-1 and HOMO(α)-2 (the top of the valence band). No such gap state appears in the ff calculation.
[c]Energy difference between HOMO(α) and HOMO(α)-2/HOMO(α)-1 for calculations without/with the finite depolarization field.
[d]Energy difference between HOMO(β) and HOMO(α)-2. No such gap state appears in the ff calculation.
[e]Energy difference between the lowest unoccupied molecular orbital, LUMO(β), and HOMO(α)-2/HOMO(α)-1 for calculations without/with the finite depolarization field.
[f]With a depolarizing electric field along the x direction at the PBE/PBE0 levels of theory as follows (magnitudes in atomic units): Sn3 (0.069/0.053), Sn7 (0.070/0.053), and Sn12 (0.052/0.038).

underestimation of the gap by the generalized-gradient functionals. Both the EWALD-ECP and H*-termination series of calculations clearly indicate that our clusters are not of sufficient size to converge the energetics. The biggest cluster size has still 1 eV too large an energy gap at the ff-EWALD-ECP/PBE level as compared to experimental value. There is very little basis-set dependence and the results of Table II are only given for our largest basis, TZVPP.

2. Neutral vacancy

Table II also indicates the location of the vacancy-induced impurity states in the band gap. For the V_O^0 system, a doubly occupied impurity state deep in the band gap is detected at both PBE [Fig. 3(b)] and PBE0 levels relatively close to the valence-band maximum, E_v. Further, unoccupied impurity related states occur close to the conduction-band minimum, E_c. These findings are in good agreement with the periodic three-parameter Becke-Lee-Yang-Parr (B3LYP) band-structure calculations of Trani *et al.*[38] using Gaussian basis sets. They find the deep level at about 1 eV above E_v and oxygen vacancy-induced structure at E_c. Also, qualitatively similar one-electron structure was found with the periodic hybrid DFT study of the V_O^0 defect in HfO_2 by Ramo *et al.*[31] Thus, both GGA and hybrid functionals, as well as both cluster and periodic models, give the same qualitative picture of the defect-induced DOS. The hybrid functionals, however, lead to much improved band gaps in periodic calculations,[31] 3.5 eV at the B3LYP level in Ref. 38 and 3.6 eV with PBE0 in Ref. 3. This is due to the contribution from the nonlocal exchange, which is necessary for adding some opening on top of the Kohn-Sham gap to bring the total gap closer to the experimentally observed one.

Experimentally, the related two first ionization levels $\varepsilon(V_O^0/V_O^{+1})$ and $\varepsilon(V_O^{+1}/V_O^{+2})$ of the oxygen vacancy have been reported to be about only 0.03–0.15 eV below the E_c of SnO_2.[2] Hence, these levels are usually termed "shallow." The DFT approach[39] for formation energies of the donor charge states and the ionization levels presumes reliable total energies. Based on these, Kılıç and Zunger[40] and Ágoston *et al.*[3] found at the local-density approximation and hybrid DFT levels, respectively, the ionization levels close to E_c, in very good agreement with the experimental result. However, Singh *et al.*[4] found in a periodic GGA+U study the V_O^0 to be a deep impurity level. The common feature in all these theoretical results is the instability of singly ionized donor state with respect to neutral or doubly ionized state at all conditions. Although there is experimental evidence for the presence of all three ionization states of the oxygen vacancy in real SnO_2 crystal, this raises the question of the presence of singly ionized V_O^+ in a perfect SnO_2 bulk crystal.

For the Sn12 model, we compared the molecular orbital (MO) coefficients for the three innermost Sn atoms, denoted "symmetric" for the two equivalent nearest-neighbor Sn atoms of the vacancy and the third, "central" Sn atom, Fig. 1. This enables the atomic contributions to the gap state to be qualitatively estimated for the V_O^0 system. The midgap impurity level has a mainly in phase, Sn s-type character at the vacancy site, with a deformed structure that has slightly less weight toward the central Sn atom than to the symmetric Sn atoms. The highest occupied MO (HOMO)-1 state that corresponds to the valence-band maximum, E_v, possesses very

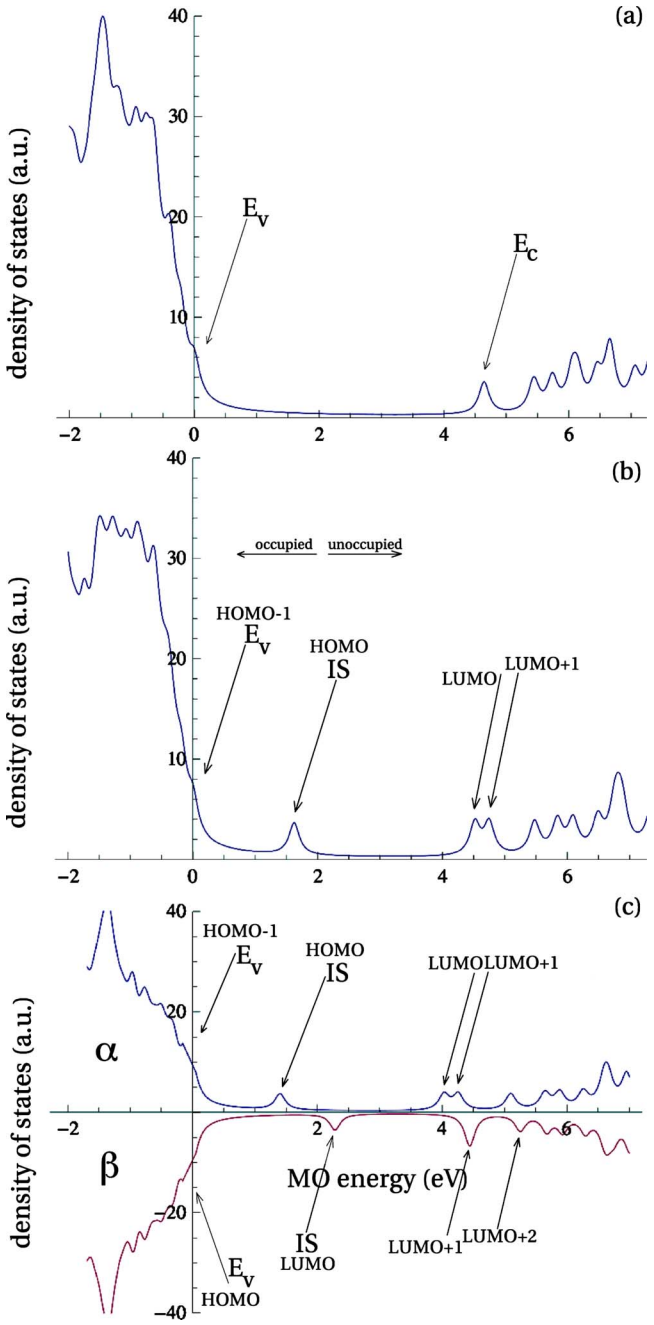

FIG. 3. (Color online) Density-of-states diagram for the ff-EWALD-ECP/Sn12 cluster model of (a) bulk SnO_2, (b) neutral oxygen vacancy V_O^0, and (c) positively charged oxygen vacancy V_O^+. E_v, E_c, and IS indicate the valence-band maximum, conduction-band minimum, and impurity state, respectively. Data from PBE/TZVPP calculation.

polarized oxygen *p*-type character. A similar qualitative inspection reveals that the lowest unoccupied MO (LUMO) state is an out-of-phase impurity state of the combination of 5*s* orbitals of the symmetric and central Sn atoms.

3. Positively charged vacancy

For the spin-polarized V_O^+ calculation, the occupied α-impurity level, singly occupied molecular orbital (SOMO), goes down in energy as compared to the doubly occupied midgap state in V_O^0. The decrease amounts to 0.4 eV for the Sn12 model at the ff-EWALD-ECP/PBE level. In this largest cluster model, additional occupied α and β states appear in the gap, below the SOMO by about 0.6 eV using the EWALD-ECP embedding, unless the depolarizing field is applied. These states have localized state characteristics but are not centered at the vacancy site. They appear to be an artifact of the spurious surface charges caused by cluster termination effects, as they disappear upon introducing the finite electric field [Fig. 3(c)]. In the largest finite-field model, the SOMO is at +1.4 (+2.1) eV above the top of the valence band, E_v, at the PBE (PBE0) level. The unoccupied β gap state moves upward in energy as compared to V_O^0 case.

TABLE III. Structural relaxation for the innermost Sn atoms for the V_O^+ and the V_O^0 systems. Data from the PBC calculations.

	V_O^+ (%)	V_O^0 (%)
Sn1	4.29	−2.85
Sn2	4.29	−2.85
Sn3	7.42	−2.03
Average	5.33	−2.58
Singh *et al.*[a]	5.6	−2.5

[a]Reference 4.

B. Structural relaxation

Table III indicates that the three closest neighbor Sn atoms around the neutral vacancy model relax inward by −2.58% of the Sn-O bond length, corresponding to 0.05 Å. Outward relaxation is observed for the V_O^+ structure by 5.33% (0.11 Å). These findings are in excellent agreement with those of Singh *et al.*[4]

C. *g* tensor

Results for the ESR *g* tensor as calculated for the V_O^+ system using different embedding models, different density functionals, and different basis sets, are listed in Table IV. Figure 4 illustrates the isotropic *g* factor obtained with the TZVPP basis set. The H*-termination and EWALD-ECP model calculations result in the *g* value slightly below the free-electron value. The H*-terminated model gives a systematically smaller *g* value, around 1.991, than the EWALD-ECP model (1.995). The results for the *g* value obtained with both the EWALD-ECP and H*-terminated models converge rapidly with the cluster size. Using the finite depolarizing field on top of the EWALD-ECP model results only in a very modest decrease in the *g* value.

The results of all the embedding schemes point to the correctness of the assignment of the experimental *g* value 2.002 by Ivanovskaya *et al.*[11] and Popescu *et al.*[12] to the V_O^+ defect. On the other hand, our results are not compatible with the assignment of experimental signal at 1.89 in Refs. 13 and 14 to this defect.

TABLE IV. Calculated g-tensor eigenvalues for the positively charged oxygen vacancy V_O^+ in SnO_2 as a function of the cluster size, DFT functional, and basis set for H^*-terminated and EWALD-ECP embedded models.

Cluster size	Embedding	Functional	Basis	g_{11}	g_{22}	g_{33}	g_{iso}
3	H^* term.	PBE	SVP	1.9854	1.9952	1.9966	1.9924
			TZVP	1.9845	1.9951	1.9960	1.9919
			TZVPP	1.9838	1.9946	1.9957	1.9914
	EWALD-ECP	PBE	SVP	1.9924	1.9945	2.0014	1.9961
			TZVP	1.9944	1.9952	2.0027	1.9974
			TZVPP	1.9911	1.9948	2.0023	1.9961
		PBE0	TZVPP	1.9915	1.9948	2.0024	1.9962
	ff-EWALD-ECP[a]	PBE	TZVPP	1.9898	1.9955	2.0020	1.9958
		PBE0	TZVPP	1.9901	1.9954	2.0021	1.9959
7	H^* term.	PBE	SVP	1.9872	1.9946	1.9960	1.9926
			TZVP	1.9864	1.9939	1.9949	1.9917
			TZVPP	1.9854	1.9933	1.9945	1.9911
	EWALD-ECP	PBE	SVP	1.9914	1.9948	1.9993	1.9952
			TZVP	1.9926	1.9952	1.9994	1.9958
			TZVPP	1.9917	1.9954	1.9995	1.9955
		PBE0	TZVPP	1.9920	1.9957	1.9998	1.9959
	ff-EWALD-ECP[a]	PBE	TZVPP	1.9910	1.9959	1.9983	1.9951
		PBE0	TZVPP	1.9914	1.9961	1.9990	1.9955
12	H^* term.	PBE	SVP	1.9923	1.9931	1.9949	1.9934
			TZVP	1.9912	1.9917	1.9933	1.9921
			TZVPP	1.9904	1.9909	1.9930	1.9914
	EWALD-ECP	PBE	SVP	1.9936	1.9957	1.9983	1.9959
			TZVP	1.9908	1.9952	1.9980	1.9947
			TZVPP	1.9909	1.9939	1.9990	1.9946
		PBE0	TZVPP	1.9911	1.9943	1.9994	1.9950
	ff-EWALD-ECP[a]	PBE	TZVPP	1.9894	1.9942	1.9986	1.9940
		PBE0	TZVPP	1.9900	1.9942	1.9991	1.9944

[a]With a depolarizing field equal to (in atomic units), for Sn3: 0.069/0.053, Sn7: 0.070/0.053, and Sn12: 0.052/0.038 along the x direction at the PBE/PBE0 levels of theory.

For comparison, when the geometry of the neutral oxygen vacancy is used for the calculations of the V_O^+ model, the g value of 2.00 is obtained at the PBE/TZVPP level, using the EWALD-ECP embedded model. Consequently, the assignment of the ESR signal around 2.002 is invariant in rather large structural changes.

The principal values of the g tensor for the ff-EWALD-ECP/Sn12/TZVPP model are 1.9911, 1.9943, and 1.9994 at the PBE level (Table IV). These correspond to the principal axes 1, 2, and 3 shown in Fig. 5, together with the spin-density distribution at the same level. A very localized spin density at the vacancy site is observed.

An insignificant difference is observed in the results of the calculations performed with the hybrid density functional (PBE0) and the GGA (PBE) methods (Table IV and Fig. 4). In a similar vein, we detected only a very small basis-set dependence in the calculations of the g tensor (Table IV). It is apparent that already the SVP basis set is sufficient for this property. These two findings point out that the g-tensor calculations for related systems can be readily pursued at the

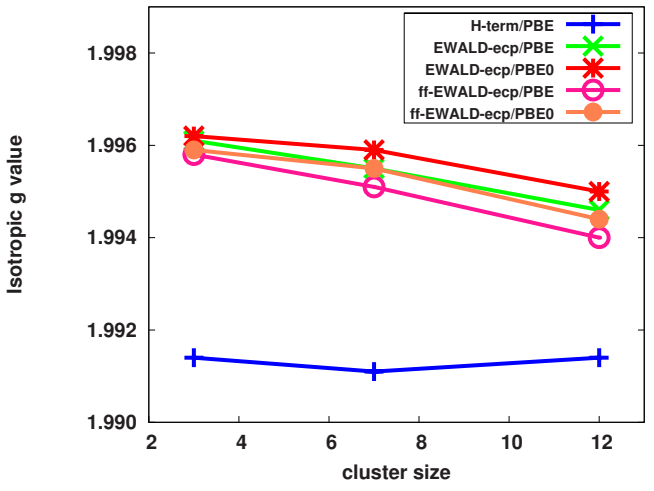

FIG. 4. (Color online) Isotropic g value as a function of the cluster model size with H^*-terminated and EWALD-ECP embedding models. TZVPP basis set is used.

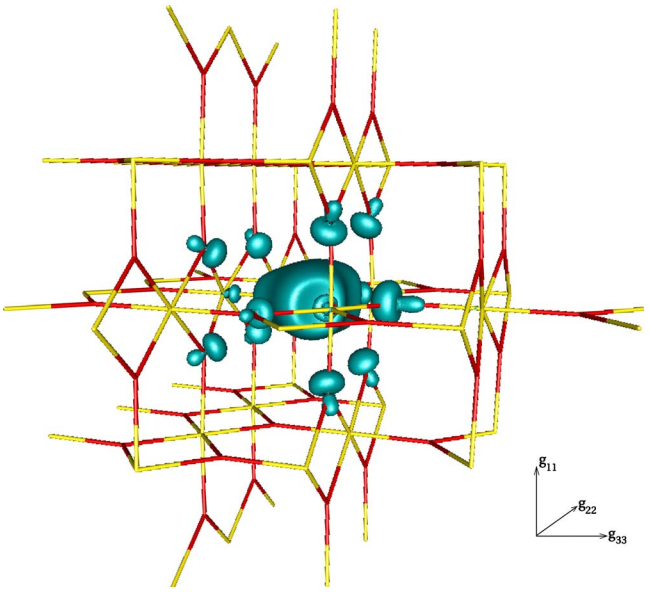

FIG. 5. (Color online) Spin density for the ff-EWALD-ECP embedded Sn12 model of the V_O^+ defect in SnO_2. The principal axis directions of the g tensor are also illustrated. Results at the PBE/TZVPP level of theory.

rather inexpensive GGA/SVP level of theory.

Test calculations (not shown) indicate that the embedding model with point charges but without the insulating ECP layer leads to erratic trends as a function of cluster size and cannot be recommended.

The weakness of the ESR signals around 2.00 correlates with the recent first-principles calculations,[3,4,40] which suggest that the V_O^+ defect is thermodynamically unstable. Different from TiO_2, where the Ti^{+3} defect exists in different variants,[41] theoretical investigations restrict the variable valency of tin atoms in SnO_2 only to Sn^{+4} or Sn^{+2} states. It is especially noteworthy that the Sn^{+4}/Sn^{+2} and V_O^0/V_O^{+2} defect states, which only may exist according to modeling, have an even number of electrons and, consequently, are ESR-silent singlets. On the other hand, reproducible paramagnetic signals with g factors in the range of 1.89–1.94 are widely observed after different treatments of the SnO_2 material.[11–14] Accordingly, some authors[12] ascribe the broad signal with $g=1.900$ to Sn^{+3} centers arising from the ionization of Sn^{+2} species.

The obvious contradiction between the theoretical stability predictions of V_O^+ and experimental ESR observations can be resolved by the fact that the evaluations of formation energies for bulk oxygen vacancies are typically performed in an otherwise perfect crystal. In experimental conditions defect complexes may exist, however, including double defects $[Sn_i\text{-}V_O]$, dioxygen vacancy structures, and various surface arrangements of V_O. The situation reminds of that in the E' center in SiO_2, where the V_O^+ defect and ESR activity are facilitated by the simultaneous split-interstitial oxygen.[42] According to our preliminary DFT calculations,[43] all the above-mentioned intrinsic defects in SnO_2 exhibit spontaneous spin polarization and therefore may be candidates for stable paramagnetic centers in this material.

D. Hyperfine coupling

The isotropic hyperfine coupling constant, A_{iso}, was calculated for the V_O^+ system. The results with respect to the

TABLE V. Isotropic hyperfine coupling for the atoms in the neighborhood of the positively charged oxygen vacancy V_O^+ in SnO_2 as a function of the cluster size and the choice of DFT functional for H^*-terminated, and EWALD-ECP-embedded models. The TZVPP basis set is used.

			$A_{iso}(^{119}Sn)$				
Embedding	Functional	Cluster size	Symmetric	Central	$A_{iso}(^{17}O_{plane})$	$A_{iso}(^{17}O_{chain})$	$A_{iso}(^{17}O_{cross})$
H^* term.	PBE	3	−1594.12	−975.96	−24.27	−43.58	−37.00
		7	−1510.45	−800.03	−19.39	−39.59	−29.68
		12	−1589.07	−489.89	−18.76	−40.62	−19.55
EWALD-ECP	PBE	3	−1275.06	−844.97	−16.24	−31.56	−26.22
		7	−1348.16	−810.07	−18.28	−30.25	−25.39
		12	−1444.78	−610.37	−17.43	−30.63	−20.78
ff-EWALD-ECP[a]	PBE	3	−1573.63	−471.66	−16.87	−36.13	−18.99
		7	−1635.84	−461.92	−18.12	−35.07	−18.08
		12	−1671.30	−366.00	−16.78	−34.07	−14.99
EWALD-ECP	PBE0	3	−1181.48	−701.11	−15.71	−31.69	−25.64
		7	−1262.97	−666.25	−17.51	−30.71	−24.69
		12	−1371.53	−496.50	−16.92	−31.57	−20.65
ff-EWALD-ECP[a]	PBE0	3	−1503.39	−545.19	−16.76	−35.08	−20.50
		7	−1465.46	−429.93	−17.58	−34.01	−19.59
		12	−1524.95	−341.07	−16.68	−33.92	−16.92

[a]With a depolarising field equal to (in a.u.), for Sn3: 0.069/0.053, Sn7: 0.070/0.053, and Sn12: 0.052/0.038 along the x direction at the PBE/PBE0 levels of theory.

cluster size and DFT functional for the H*-terminated and EWALD-ECP models are listed in Table V. Convergence is illustrated for the EWALD-ECP model with the different basis sets using the PBE and (with the TZVPP basis set) PBE0 functionals, in Fig. 6. Similarly to the g tensor case, the EWALD model without ECP insulation is unreliable, and the results are not shown.

Calculations performed with the H*-terminated model give a larger A_{iso} as compared to the EWALD-ECP model. The convergence of the results is faster with the EWALD-ECP embedding than with H* termination. A moderate dependence on the cluster size remains with EWALD-ECP calculations. The results are far from convergence for $A_{iso}(^{17}O_{cross})$ at the Sn12 model size unlike for the other couplings, where signs of saturation are visible in the change between Sn7 and Sn12 models. The relative change in the EWALD-ECP results due to introducing the finite depolarizing field is larger than for the g tensor.

The results obtained with the PBE0 density functional for the EWALD-ECP model give a distinctly smaller $A_{iso}(^{119}Sn)$ as compared the corresponding calculation with the PBE functional. Figure 6 shows that there is a rather big difference in the results from the small SVP basis set and TZVP/TZVPP sets. The latter are similar in the atomic core region and consequently give similar hyperfine couplings. TZVP and TZVPP are in general not fully converged basis sets for hyperfine coupling calculations, and a more flexible core should still be used for comparison with the eventual experiment. We note that for quantitative predictions of $A_{iso}(^{119}Sn)$ relativistic effects should also be included.[44,45]

IV. CONCLUSIONS

Based on geometry optimizations in periodic plane-wave pseudopotential DFT calculations, we have constructed finite, nonstoichiometric cluster models of the defect-free bulk SnO_2, as well as a neutral oxygen vacancy (V_O^0), and a singly positively charged oxygen vacancy (V_O^+) therein. DFT calculations of the finite models have been carried out with the dangling bonds terminated by pseudohydrogen atoms as well as with the cluster embedded in a large array of point charges fitted to reproduce, within the cluster volume, the Madelung potential of the infinite defect-free lattice. A variant of the embedding procedure was considered where the bare point charges of the cationic lattice sites closest to the cluster were replaced by effective core potentials, to avoid leakage of the negative charge from the cluster to the point charges. A finite electric field was applied to approximately eliminate spurious polarization effect due to using finite cluster models. The cluster calculations were performed with both GGA and hybrid exchange-correlation functionals, as well as with Gaussian basis sets of different quality.

The V_O^+ system has one unpaired electron. DFT calculations of the ESR g tensor and the isotropic hyperfine coupling constant (A_{iso}), for nuclei in the neighborhood of the vacancy, were carried out to resolve the situation with respect to mutually disagreeing experimental assignments of the ESR spectra of this system. Due to the localized spin-density distribution around the vacancy, the g tensor and A_{iso}

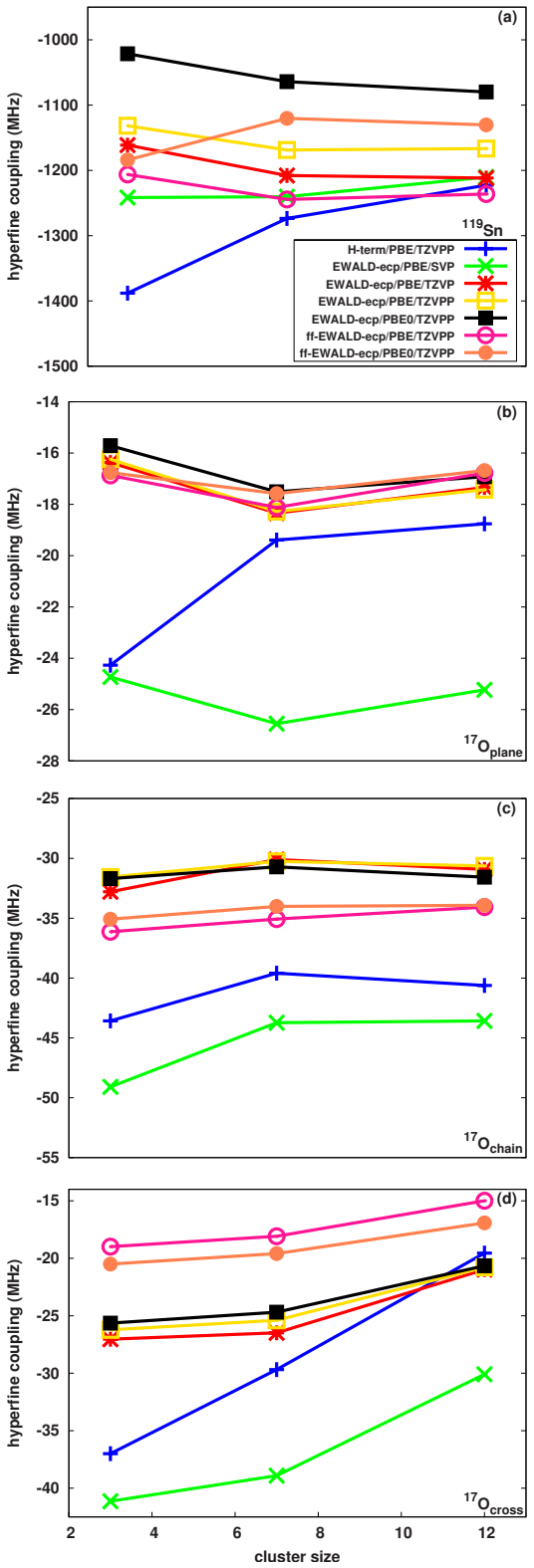

FIG. 6. (Color online) Convergence of hyperfine coupling for the EWALD-ECP terminated cluster models of positively charged oxygen vacancy V_O^+ in SnO_2. (a) $A_{iso}(^{119}Sn)$, (b) $A_{iso}(^{17}O_{plane})$, (c) $A_{iso}(^{17}O_{chain})$, (d) $A_{iso}(^{17}O_{cross})$, with the SVP, TZVP, and TZVPP basis sets with PBE functional, as well as TZVPP basis set with the PBE0 functional. Symmetric and central tin atoms closest to the vacancy have been averaged over. The H*-terminated results are obtained at the PBE/TZVPP level.

for all but one type of ^{17}O sites in the vicinity of the vacancy, were found to be converged with respect to the cluster size for our largest model containing 12 tin atoms.

The dependence on the exchange-correlation functional and the basis set were found to be small for the g tensor, whereas the hyperfine coupling constants expectedly exhibit a larger sensitivity. The electrostatic embedding procedure with the effective core potentials placed at the perimeter of the cluster, was found to lead to numerically stable ESR parameters and improved convergence with respect to the cluster size, as compared to pseudohydrogen-terminated clusters. On the other hand, embedding without the effective core potentials led to convergence problems and clearly erroneous results for the ESR parameters, presumably due to charge leakage from the cluster to the closest cationic point charges.

The calculated isotropic g value strongly corroborates two earlier assignments of the weak ESR signal of V_O^+ around 2.00. In contrast, the strong experimental signal at 1.89 reported in a number of preceeding papers, is likely to be caused by some other paramagnetic defect. Apparently the V_O^+ defect is less stable than these other defects that give stronger signals. Indeed, recent theoretical investigations point to thermodynamic instability of the V_O^+ defect in an otherwise perfect crystal. Consequently, the appearance of the V_O^+ signal in ESR points to the presence of simultaneous, stabilizing imperfections in the SnO_2 structure. There are no experimental reports of A_{iso} for the V_O^+ system.

Unlike the magnetic parameters, the energetic properties are not converged with the cluster size in the present bulk cluster model. This is seen not only in the one-electron levels but also in total energies. In models of the neutral vacancy, a doubly occupied level induced by the vacancy appears within the HOMO-LUMO gap. Ionization shifts and splits the level to its spin components. In the present cluster calculations of the spin-polarized V_O^+ model, the application of the finite depolarization field is found to be necessary for obtaining a qualitatively correct one-electron level structure, which is in agreement with that from other published studies. It is, however, unable to reproduce the relative energies of the ionization levels. As the performance of the cluster models for the localized magnetic properties is promising, we are pursuing such studies for bulk and surface models of related semiconductor systems.

ACKNOWLEDGMENTS

We acknowledge Nino Runeberg, CSC, Espoo, Finland, for his help with the GAUSSIAN software. N.Ö. and J.V. belong to the Finnish Center of Excellence in Computational Molecular Science (CMS). Financial support was obtained from the Research Funds (N.Ö. and J.V.) and the Research Foundation (N.Ö.) of the University of Helsinki. Computational resources were partially provided by the Center for High-Performance Computing and Networking CSC, Espoo, Finland.

*Corresponding author; juha.vaara@oulu.fi

[1] J. Watson, K. Ihokura, and C. S. V. Coles, Meas. Sci. Technol. **4**, 711 (1993).
[2] S. Samson and C. G. Fonstad, J. Appl. Phys. **44**, 4618 (1973).
[3] P. Ágoston, K. Albe, R. M. Nieminen, and M. J. Puska, Phys. Rev. Lett. **103**, 245501 (2009).
[4] A. K. Singh, A. Janotti, M. Scheffler, and C. G. Van de Walle, Phys. Rev. Lett. **101**, 055502 (2008).
[5] C. Di Valentin and G. Pacchioni, Modell. Simul. Mater. Sci. Eng. **17**, 084005 (2009).
[6] C. J. Pickard and F. Mauri, Phys. Rev. Lett. **88**, 086403 (2002).
[7] E. S. Kadantsev and T. Ziegler, J. Phys. Chem. A **113**, 1327 (2009).
[8] Q. Huo, Colloids Surf., B **59**, 1 (2007).
[9] M. Pumera, S. Sanchez, I. Ichinose, and J. Tang, Sens. Actuators B **123**, 1195 (2007).
[10] Z. H. Xiong, D. Wu, Z. V. Vardeny, and J. Shi, Nature (London) **427**, 821 (2004).
[11] M. Ivanovskaya, P. Bogdanov, G. Faglia, P. Nelli, G. Sberveglieri, and A. Taroni, Sens. Actuators B **77**, 268 (2001).
[12] D. Amalric Popescu, J. M. Herrmann, A. Ensuque, and F. Bozon-Verduraz, Phys. Chem. Chem. Phys. **3**, 2522 (2001).
[13] C. Canevali, N. Chiodini, P. Di Nola, F. Morazzoni, R. Scotti, and C. L. Bianchi, J. Mater. Chem. **7**, 997 (1997).
[14] N. Chiodini, C. Canevali, F. Morazzoni, R. Scottia, and C. L. Bianchi, Int. J. Inorg. Mater. **2**, 355 (2000).
[15] T. T. Rantala, T. S. Rantala, and V. Lantto, Surf. Sci. **420**, 103 (1999).
[16] V. Milman, B. Winkler, J. A. White, C. J. Pickard, M. C. Payne, E. V. Akhmatskaya, and R. H. Nobes, Int. J. Quantum Chem. **77**, 895 (2000).
[17] S. J. Clark, M. D. Segall, C. J. Pickard, P. J. Hasnip, M. I. J. Probert, K. Refson, and M. C. Payne, Z. Kristallogr. **220**, 567 (2005).
[18] D. Vanderbilt, Phys. Rev. B **41**, 7892 (1990).
[19] H. J. Monkhorst and J. D. Pack, Phys. Rev. B **13**, 5188 (1976).
[20] J. P. Perdew, K. Burke, and M. Ernzerhof, Phys. Rev. Lett. **77**, 3865 (1996); **78**, 1396(E) (1997).
[21] J. P. Perdew, J. A. Chevary, S. H. Vosko, K. A. Jackson, M. R. Pederson, D. J. Singh, and C. Fiolhais, Phys. Rev. B **46**, 6671 (1992).
[22] V. B. Sulimov, P. V. Sushko, A. H. Edwards, A. L. Shluger, and A. M. Stoneham, Phys. Rev. B **66**, 024108 (2002).
[23] J. Sauer, Chem. Rev. **89**, 199 (1989).
[24] M. Klintenberg, S. E. Derenzo, and M. J. Weber, Comput. Phys. Commun. **131**, 120 (2000).
[25] S. E. Derenzo, M. M. Klintenberg, and M. J. Weber, J. Chem. Phys. **112**, 2074 (2000).
[26] J. L. Pascual and L. G. M. Petterson, Chem. Phys. Lett. **270**, 351 (1997).
[27] A. Bergner, M. Dolg, W. Kuechle, H. Stoll, and H. Preuss, Mol. Phys. **80**, 1431 (1993).
[28] D. L. Pechkis, E. J. Walter, and H. Krakauer, J. Chem. Phys. **131**, 184511 (2009).

[29] J. E. Harriman, *Theoretical Foundations of the Electron Spin Resonance* (Academic Press, New York, 1978).
[30] M. J. Frisch, G. W. Trucks, H. B. Schlegel, G. E. Scuseria, M. A. Robb, J. R. Cheeseman, J. A. Montgomery, Jr., T. Vreven, K. N. Kudin, J. C. Burant, J. M. Millam, S. S. Iyengar, J. Tomasi, V. Barone, B. Mennucci, M. Cossi, G. Scalmani, N. Rega, G. A. Petersson, H. Nakatsuji, M. Hada, M. Ehara, K. Toyota, R. Fukuda, J. Hasegawa, M. Ishida, T. Nakajima, Y. Honda, O. Kitao, H. Nakai, M. Klene, X. Li, J. E. Knox, H. P. Hratchian, J. B. Cross, V. Bakken, C. Adamo, J. Jaramillo, R. Gomperts, R. E. Stratmann, O. Yazyev, A. J. Austin, R. Cammi, C. Pomelli, J. W. Ochterski, P. Y. Ayala, K. Morokuma, G. A. Voth, P. Salvador, J. J. Dannenberg, V. G. Zakrzewski, S. Dapprich, A. D. Daniels, M. C. Strain, O. Farkas, D. K. Malick, A. D. Rabuck, K. Raghavachari, J. B. Foresman, J. V. Ortiz, Q. Cui, A. G. Baboul, S. Clifford, J. Cioslowski, B. B. Stefanov, G. Liu, A. Liashenko, P. Piskorz, I. Komaromi, R. L. Martin, D. J. Fox, T. Keith, M. A. Al-Laham, C. Y. Peng, A. Nanayakkara, M. Challacombe, P. M. W. Gill, B. Johnson, W. Chen, M. W. Wong, C. Gonzalez, and J. A. Pople, GAUSSIAN 03, Revision C.02, Gaussian, Inc., Wallingford, CT, 2004.
[31] D. Muñoz Ramo, J. L. Gavartin, A. L. Shluger, and G. Bersuker, Phys. Rev. B **75**, 205336 (2007).
[32] V. Gomzi and J. N. Herak, Chem. Phys. **333**, 112 (2007).
[33] O. L. Malkina, J. Vaara, B. Schimmelpfenning, M. Munzarová, V. G. Malkin, and M. Kaupp, J. Am. Chem. Soc. **122**, 9206 (2000).
[34] P. W. Atkins and R. S. Friedman, *Molecular Quantum Mechanics* (Oxford University Press, Oxford, 1997).
[35] A. Schäfer, H. Horn, and R. Ahlrichs, J. Chem. Phys. **97**, 2571 (1992).
[36] A. Schäfer, C. Huber, and R. Ahlrichs, J. Chem. Phys. **100**, 5829 (1994).
[37] G. Pacchioni, A. M. Ferrari, and G. Ierano, Faraday Discuss. **106**, 155 (1997).
[38] F. Trani, M. Causá, D. Ninno, G. Cantele, and V. Barone, Phys. Rev. B **77**, 245410 (2008).
[39] C. G. Van de Walle and J. Neugebauer, J. Appl. Phys. **95**, 3851 (2004).
[40] C. Kılıç and A. Zunger, Phys. Rev. Lett. **88**, 095501 (2002).
[41] Y. Hajimoto, E. Yamaka, M. Nagasawa, and S. Shionoya, Phys. Lett. **23**, 50 (1966).
[42] C. M. Carbonaro, V. Fiorentini, and F. Bernardini, Phys. Rev. Lett. **86**, 3064 (2001).
[43] V. Golovanov (unpublished).
[44] S. Komorovský, M. Repiský, O. L. Malkina, V. G. Malkin, I. Malkin, and M. Kaupp, J. Chem. Phys. **124**, 084108 (2006).
[45] S. Blügel, H. Akai, R. Zeller, and P. H. Dederichs, Phys. Rev. B **35**, 3271 (1987).